Efficient clearance of periodontitis pathogens by S. gordonii membrane-coated H_2O_2 self-supplied nanocomposites in a “Jenga” style

Cao, Qinghua; Xiao, Xiang; Tao, Chengcheng; Shi, Rui; Lv, Rui; Guo, Ruochen; Li, Xinyi; Sui, Baiyan; Liu, Xin; Liu, Jian

Published in:
Biomaterials Science

DOI:
10.1039/d3bm00641g

Publication date:
2023

Biomaterials Science

ROYAL SOCIETY OF CHEMISTRY

PAPER

View Article Online
View Journal | View Issue

Cite this: *Biomater. Sci.*, 2023, **11**, 5680

Efficient clearance of periodontitis pathogens by *S. gordonii* membrane-coated H_2O_2 self-supplied nanocomposites in a "Jenga" style†

Qinghua Cao,[a] Xiang Xiao,[a] Chengcheng Tao,[a] Rui Shi,*[a,b] Rui Lv,[a] Ruochen Guo,[a] Xinyi Li,[a] Baiyan Sui,[c] Xin Liu[c] and Jian Liu *[a]

Received 16th April 2023,
Accepted 4th July 2023

DOI: 10.1039/d3bm00641g

rsc.li/biomaterials-science

As a key pathogen of periodontitis, *P. gingivalis* requires support of the initial colonizing bacterium (*S. gordonii* preferably) to form symbiotic biofilms on gingival tissues with enhanced antibiotic resistance. Here, we report a new strategy to treat periodontitis biofilms with *S. gordonii* membrane-coated H_2O_2 self-supplied nanocomposites (ZnO_2/Fe_3O_4@MV NPs) in a "Jenga" style. Integration of our special MV coatings enables selectively enhanced internalization of the cargos in *S. gordonii*, thus inducing severe damage to the foundational bacterial layer and collapse/clearance of symbiotic biofilms consequently. This strategy allows us to clear the symbiotic biofilms of *S. gordonii* and *P. gingivalis* with active hydroxyl radicals (•OH) derived from ZnO_2–Fe_3O_4@MV NPs in a H_2O_2 self-supplied, nanocatalyst-assisted manner. This "Jenga-style" treatment provides a cutting-edge proof of concept for the removal of otherwise robust symbiotic biofilms of periodontitis where the critical pathogens are difficult to target and have antibiotic resistance.

1. Introduction

The oral cavity has the second largest microflora with over 700 species of bacteria, only less than that in the intestinal tract in the human body.[1] The unique structure of the oral cavity allows for microbial colonization and symbiotic biofilm formation in the tooth gaps and gingival sulci.[2] The process of symbiotic biofilm (dental plaque) formation involves multiple kinds of bacteria in the oral cavity, according to some certain sequences: for instance, the initial colonizing bacteria are accumulated *in situ* with the assistance of saliva and the gingival crevicular fluid; then, the interactions between the initial colonizing bacteria and the following-up bacteria through adhesins will mediate secondary colonization, *etc.*[3,4] Periodontitis is typically a chronic disease caused by plaque accumulation, which can lead to inflammatory infiltration, periodontal collagen breakdown, and even tooth loss.[5] *Porphyromonas gingivalis*, a key pathogen of periodontitis, is a representative of secondary colonizing bacteria in dental plaque.[6,7] Even at low abundance (<0.01%), *P. gingivalis* can invade and destroy gingival tissues; it can also be associated with systemic disorders such as Alzheimer's disease, colorectal cancer, and adverse pregnancy outcomes.[8–10] *Streptococcus gordonii* typically acts as the initial colonizing bacterium, analogous to the "vanguard" of dental plaque, by taking advantage of varieties of adhesive proteins of its own. It can offer nutrient supplies and an adhesion basis for *P. gingivalis* secondary colonization.[11,12] A previous report has suggested a positive preference of *P. gingivalis* entering *S. gordonii* biofilm in comparison to the other oral *Streptococcus* biofilms.[13] The recognition may be mediated by *P. gingivalis* fimbriae interacting with the SspA/B streptococcal surface polypeptide and handover of heme coordinated by several heme-binding proteins between these two types of bacteria.[14,15] The alliance of *P. gingivalis* and *S. gordonii* essentially enhances their resistance to antibiotics or unfriendly stimuli from the external environment.[16] The conventional treatments against periodontitis include physical removal with special dental tools, such as curettes, and systemic antibiotic therapies.[17] However, they suffer from relatively low efficacy and unavoidable remains of pathogenic bacteria, usually leading to risks of periodontitis recurrence or a bad loop of antibiotic resistance. Therefore, there is a great need to develop new antibiofilm methods

[a]*Institute of Functional Nano & Soft Materials (FUNSOM), Jiangsu Key Laboratory for Carbon-Based Functional Materials & Devices, Soochow University, 199 Ren'ai Rd, Suzhou 215123, Jiangsu, P. R. China. E-mail: jliu@suda.edu.cn*
[b]*University of Groningen and University Medical Center Groningen, Department of Biomedical Engineering, Antonius Deusinglaan 1, 9713 AV Groningen, The Netherlands. E-mail: r.shi@umcg.nl*
[c]*Department of Dental Materials, Shanghai Biomaterials Research & Testing Center, Shanghai Ninth People's Hospital, Shanghai Jiao Tong University School of Medicine, College of Stomatology, Shanghai Jiao Tong University, National Center for Stomatology, National Clinical Research Center for Oral Diseases, Shanghai Key Laboratory of Stomatology, Shanghai, 200011, P.R. China*
† Electronic supplementary information (ESI) available. See DOI: https://doi.org/10.1039/d3bm00641g

targeting colonization of symbiotic pathogenic bacteria to treat periodontitis with a high efficiency.

The development of nanomedicines against biofilms is an active research area, promising better solutions to address the challenge of drug resistance.[18,19] Nanomaterial-based chemodynamic therapies (CDTs) have been developed by taking advantage of nanocatalyst-assisted Fenton or Fenton-like reactions, which can generate highly toxic hydroxyl radicals (˙OH) under acidic conditions to kill bacteria.[20] Interestingly, the pH of oral biofilms is typically reduced to less than 5.0 after intake of food, matching the weakly acidic requirement of Fenton reactions.[21] The therapies in the nano-formulations usually feature a small particle size and high specific surface area, facilitating penetration/destruction of microbial membranes with the assistance of ˙OH.[22,23] Bacterial membrane vesicles are typically in diameters ranging from 20 nm to 400 nm, composed of phospholipid bilayers containing intimal proteins, cytoplasmic proteins, DNA, RNA, and metabolic molecules. They are attributed to nutrient or information exchanges between bacterial cell-to-cell communications.[24–26] Many studies suggested that parent cells tend to re-acquire large quantities of substances coated by their own membrane vesicles by internalization or membrane fusion, which enables selectively targeted delivery.[27,28] In comparison to traditional liposomal formulations, bacterial membrane vesicles are relatively easier to harvest in large quantities and display functional biomolecules by bacterial engineering, thus promising wide applications in biomedicine.

Here, we report a new concept to treat periodontitis biofilms with *S. gordonii* membrane-coated H_2O_2 self-supplied nanocomposites (Scheme 1). It features selectively targeted delivery of our nanotherapeutics into *S. gordonii*, inducing severe damage to the foundational bacterial layer and collapse/clearance of symbiotic biofilms consequently. To draw an analogy, it allows for effective removal of symbiotic biofilms in a "Jenga" style. As shown in Scheme 1a, ZnO_2 nanoparticles were synthesized and then assembled with Fe_3O_4 nanoparticles on the shell, followed by encapsulation with *S. gordonii* membrane vesicles (ZnO_2/Fe_3O_4@MV NPs). The nanotherapeutics can be delivered onto the periodontitis biofilms and taken up by *S. gordonii* predominantly. Then, ZnO_2 NPs decompose to release H_2O_2, followed by generation of highly active ˙OH by a Fe_3O_4 NP-catalyzed Fenton reaction to kill bacteria. The damage of *S. gordonii* dramatically undermines the robustness of symbiotic anti-biofilms, leading to the final clearance of periodontitis pathogens (Scheme 1b). We have demonstrated the effect of selectively enhanced internalization of the cargos with our special MV coatings in *S. gordonii*, in comparison to *P. gingivalis* by flow cytometry and fluorescence microscopy. Both *in vitro* and *ex vivo* experiments have suggested that the symbiotic biofilms of *S. gordonii* and *P. gingivalis* can be cleared by ZnO_2–Fe_3O_4@MV NPs, better than the other control treatments. This work not only presents new therapeutics to treat periodontitis with a high efficacy, but also highlights a new method to control different bacterial types/abundances and modify their symbiotic biofilms in a "Jenga" style.

2. Materials and methods

2.1. Materials

Zinc acetate dihydrate ($Zn(OAc)_2$), iron acetylacetonate ($Fe(acac)_3$), poly(vinyl pyrrolidone) (PVP), 1,2-hexadecanediol, oleic acid (OA), oleyl amine (OM), benzyl ether, and hemin were purchased from Sigma-Aldrich (St Louis, Mo, USA). 3-(3,4-Dihydroxyphenyl) propanoic acid (DHCA) was purchased from Thermo Fisher-Alfa Aesar (Waltham, MA, USA). Ethanol, hydrogen peroxide (H_2O_2), hexane, glucose, yeast extract, tetracycline and cyclohexane were provided by Sinopharm Chemical Reagent Co., Ltd (Shanghai, China). Syto9 green fluorescent (Syto9), L-cysteine hydrochloride, dipotassium hydrogen phosphate (K_2HPO_4), vitamin K1, 3,3′,5,5′-tetramethylbenzidine (TMB), tetrahydrofuran (THF), sodium hydroxide (NaOH), 5-(and-6)-carboxyfluorescein and succinimidyl ester (5(6)-FAM), hexidium iodide (HI), 2′,7′-dichlorofluorescin diacetate (DCFH-DA) and dimethyl sulfoxide (DMSO) were obtained from Aladdin Biochemical Technology Co., Ltd (Shanghai, China). Tryptone soy broth (TSB) was obtained from Hangzhou Microbial Reagent Co., Ltd (Hangzhou, China). Tissue AutoFluo Quencher was purchased from Applygen Gene Technology Co., Ltd (Beijing, China). 1,1-Dioctadecyl-3,3,3,3-tetramethylindocarbocyanine iodide (DiI) and Hydrogen Peroxide (H_2O_2) Content Assay Kits were purchased from Solarbio Technology Co., Ltd (Beijing, China). Egg-yolk L-α-phosphatidylcholine (EPC) was purchased from Avanti Polar Lipids (Alabaster, AL). Omni-PAGE Hepes-Tris Gels were purchased from Epizyme Biomedical Technology Co., Ltd (Shanghai, China). Coomassie Blue Staining Solution was purchased from Macklin Biochemical Technology Co., Ltd (Shanghai, China). All chemicals were used without further purification. Ultrapure water (18.2 MΩ) was used throughout the experiments.

2.2. Synthesis of ZnO_2 and Fe_3O_4 NPs

ZnO_2 [29] and Fe_3O_4 [30] nanoparticles were prepared according to previously published methods. To prepare ZnO_2 nanoparticles, 0.1 g of $Zn(OAc)_2$ (99%) and 0.15 g of PVP (M_w = 10 000) were dissolved in 5.0 mL of water. Then, 0.5 mL of H_2O_2 (30 wt%) was added into the mixture under sufficient stirring. After 24 h of reaction, the PVP-modified ZnO_2 nanoparticles were washed 3 times and then redispersed in ultrapure water.

For the preparation of Fe_3O_4 nanoparticles, $Fe(acac)_3$ (2 mmol), 1,2-hexadecanediol (10 mmol), OA (6 mmol), OM (6 mmol), and benzyl ether (20 mL) were mixed and magnetically stirred under an atmosphere of nitrogen. The mixture was heated at 200 °C for 2 h and then heated to 300 °C under nitrogen for 1 h. After the black mixture was cooled to room temperature, ethanol (40 mL) was added to the mixture. The black substance was precipitated and separated by centrifugation (13 000*g*, 10 min). The black product was dissolved in hexane in the presence of OA (0.05 mL) and OM (0.05 mL). The product was precipitated with ethanol, centrifuged to remove the supernatant (13 000*g*, 10 min), washed several times, and then dispersed in THF.

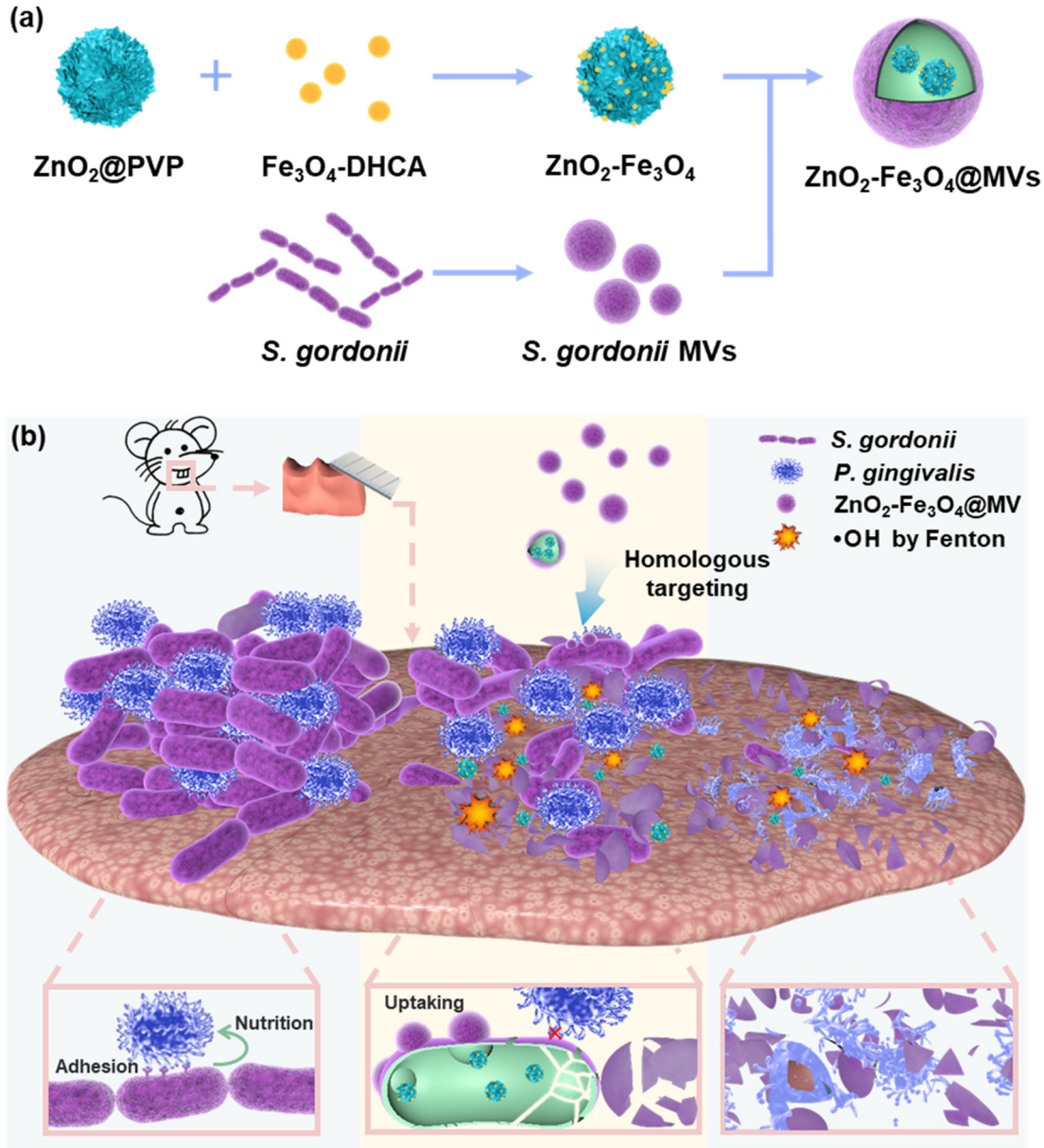

Scheme 1 Schematic illustrations of (a) preparation of ZnO_2–Fe_3O_4@MV NPs and (b) the treatment of periodontitis symbiotic biofilms by the "Jenga-style".

2.3. Synthesis of ZnO_2–Fe_3O_4 NPs

DHCA (50 mg) was dissolved in 6 mL of THF, slowly added to a THF solution containing 20 mg of Fe_3O_4 NPs (20 mg mL^{-1}), and then magnetically stirred under an atmosphere of nitrogen. The mixture was slowly heated to 50 °C for 3 h, and magnetically stirred until it cooled to room temperature. 0.5 mL of NaOH (0.5 mmol) was added to precipitate the black product. It was washed 3 times and then dispersed in ultrapure water.

Five milliliters of ZnO_2 (1 mg mL^{-1}) were added to 1 mL of Fe_3O_4–DHCA (10 mg mL^{-1}) aqueous solution under ultrasound for 5 min. The mixture was then stirred with a magnetic agitator (1000 rpm for 12 h), washed with water 3 times to remove excess Fe_3O_4–DHCA, and stored in ultrapure water.

2.4. Bacterial and cell culture

Porphyromonas gingivalis (ATCC 33277) from frozen stock was inoculated in Columbia agar supplemented with 5 v/v% horse blood at 37 °C under anaerobic conditions (21% CO_2, 79% N_2). One single colony was transferred into 40 mL of trypticase soy broth (TSB) supplemented with yeast extract (5 mg mL^{-1}), hemin stock (1 mL), L-cysteine hydrochloride (0.5 mg mL^{-1}) and vitamin K1 (1 mg mL^{-1}) and maintained under anaerobic conditions at 37 °C for 7–9 days. The hemin stock solution consisted of hemin (5 mg mL^{-1}) and K_2HPO_4 (17.4 mg mL^{-1}). *Streptococcus gordonii* (ATCC 10558) was inoculated in Columbia agar supplemented with 5 v/v% horse blood at 37 °C in ambient air. One colony was taken from the Columbia agar

plate and transferred into 8 mL of trypticase soy broth (TSB) supplemented with yeast extract (5 mg mL^{-1}) and glucose (5 mg mL^{-1}) and maintained for 12 h.

HUVECs and 3T3 cells were used in the cytotoxicity test. All cells were incubated in DMEM containing 10% FBS, 100 U mL^{-1} penicillin and 100 μg mL^{-1} streptomycin at 37 °C under a humidified atmosphere containing 5% CO_2.

2.5. Isolation of *S. gordonii* membrane vesicles

To collect membrane vesicles (MVs), *S. gordonii* was incubated in TSB for approximately 24 h to obtain a concentration of 1×10^8 CFU mL^{-1}. Then, the bacterial culture was centrifuged at 1800*g* for 10 min to remove bacteria. Then, the supernatant was concentrated 3 times with a 100 kDa molecular weight ultrafiltration tube. Finally, *S. gordonii* MVs in the concentrated supernatant were collected by ultracentrifugation (Beckmann, Optima XPN-100 ultracentrifuge, SW41 Ti) at 150 000*g* and 4 °C for 2 h. The obtained precipitates were resuspended in sterile 1× PBS and stored at −80 °C for subsequent experiments.

2.6. Preparation of ZnO_2–Fe_3O_4@MV NPs

Briefly, ZnO_2–Fe_3O_4 NPs were centrifuged and resuspended in 1× PBS. Then, the *S. gordonii* MVs collected above were mixed with ZnO_2–Fe_3O_4 NPs at a volume ratio of 1 : 3, with ultrasonic pretreatment for 3 min. The mixture was squeezed dozens of times using a hand-held mini-extruder with a 400 nm polycarbonate porous membrane. Then, the mixture was centrifuged at 3500*g* for 10 min at 4 °C to precipitate the nanocomposites. After removal of the supernatant, the nanocomposites were concentrated and suspended in 1× PBS for subsequent use.

2.7. Characterization of ZnO_2–Fe_3O_4@MV NPs

For transmission electron microscopy (TEM) characterization, ZnO_2–Fe_3O_4 NPs and ZnO_2–Fe_3O_4@MV NPs suspended in PBS were placed onto a carbon-coated copper grid. After evaporation of PBS under ambient conditions, high-resolution TEM, high-angle annular dark-field scanning TEM (HAADF-STEM) and energy dispersive X-ray (EDX) were performed using a TALOS 200X microscope operated at 200 kV (FEI, USA). The hydrodynamic size and surface zeta potential of Fe_3O_4–DHCA, ZnO_2, ZnO_2–Fe_3O_4 NPs, *S. gordonii* MVs and ZnO_2–Fe_3O_4@MV NPs were measured with a Zetasizer Nano ZS (Malvern Instruments, UK). All measurements were carried out in triplicate at room temperature. X-ray powder diffraction patterns were collected using a Philips X'pert PRO MPD diffractometer applying Cu Kα radiation (λ = 0.15406 nm). The operation voltage and current were maintained at 40 kV and 40 mA, respectively. UV-vis-NIR absorbance spectra were recorded using a PerkinElmer Lambda 750 UV-vis-NIR spectrophotometer. The total protein content of ZnO_2–Fe_3O_4@MVNPs was quantified with a BCA assay (Thermo Scientific).

The release of Fe and Zn ions from ZnO_2–Fe_3O_4@MV NPs was determined by dialysis (14 kDa). The aqueous solution of ZnO_2–Fe_3O_4@MV NPs was dialyzed with acetate buffer (pH 5.5 and pH 7.4). Then, the concentrations of Fe and Zn ions at different time points were measured by inductively coupled plasma-optical emission spectrometry (ICP-OES). H_2O_2 release of ZnO_2 NPs was measured using commercial H_2O_2 assay kits.

SDS-PAGE was used to verify the protein of the isolated *S. gordonii* MVs and ZnO_2–Fe_3O_4@MV NPs. Protease inhibitors and RIPA lysate were added to 200 μL of each sample to be tested; the mixture was ultrasonically lysed 30 times on ice (each ultrasonication 3 s, interval 7 s) and incubated for 10 min at 95 °C prior to electrophoretic separation on commercial polyacrylamide gel under a constant voltage of 220 V in running buffer. Gels were immersed and incubated with Coomassie Brilliant Blue staining solution; then, an eluent was used to remove unbound stains until the protein bands were clear.

2.8. Calculation of the ·OH generation ability of ZnO_2–Fe_3O_4@MV NPs

The calculation of the ·OH production of ZnO_2–Fe_3O_4@MV NPs was conducted based on the oxidation of TMB. First, ZnO_2–Fe_3O_4@MV NPs (20 μg mL^{-1}) were dispersed in TMB solution (0.25 mM) at different pH values (4.5, 5.0, 5.5 and 7.4), and the UV-vis absorption of various samples was recorded using a BioTek Multimode Reader after 30 min of incubation. The increase in ·OH production mediated by other groups was investigated using the same method as above. Different concentrations of ZnO_2–Fe_3O_4@MV NPs (0, 5, 10 and 20 μg mL^{-1}) were also dispersed in PBS buffer (pH 5.0). After addition of 100 μL of TMB solution, the mixture was incubated at 37 °C for 30 min before UV-vis absorbance measurements.

2.9. Cytotoxicity investigation of ZnO_2–Fe_3O_4@MV NPs

The *in vitro* cytotoxicity of ZnO_2–Fe_3O_4@MV NPs was assessed on cultured HUVECs and 293T cells. At 70% confluency, the cells were harvested by adding an EDTA–trypsin solution, centrifuged at 500*g* for 5 min and resuspended in DMEM–HG. The cells were seeded in 96-well plates (1×10^4 cells, 100 μL per well) and grown for 24 h. After overnight incubation, the culture medium was replaced with the fresh medium containing different concentrations of ZnO_2–Fe_3O_4@MV NPs (0, 1.56, 3.13, 6.25, 12.50, 25, 50, 100, and 200 μg mL^{-1}). After another 24 h, cell viability was assessed using the CellTiter-GlO (CTG) luminescence cell viability assays according to the standard procedure.

2.10. Minimum inhibitory concentration (MIC)

The antibacterial drug tetracycline is widely used in the treatment of periodontitis infection. The MIC values were determined by the microdilution method in 96-well microplates according to a previous study.[31] Briefly, *S. gordonii* was collected by centrifugation at 1500*g* for 5 min and washed twice with 1× PBS. The bacteria were resuspended in 10 mL of TSB to a concentration of 1×10^7 CFU mL^{-1}, as determined by plate counting in a series of separate experiments. Next, the MIC values of tetracycline in solutions were measured by making twofold serial dilutions; the concentration range after serial dilution was 0.78–100 μg mL^{-1}. One hundred microliters

of these dilutions in 96-well plates were supplemented with 100 μL of *S. gordonii* suspensions in TSB (finally diluted to 5×10^6 CFU mL^{-1}). After incubation for 24 h at 37 °C, the OD_{600} of the cell suspension in each well was measured using a microplate reader (BioTek). The MIC of tetracycline (3 μg mL^{-1}) was determined as the lowest antibiotic concentration by the absorbance measurements of *S. gordonii* suspensions (OD_{600} < 0.1). This concentration of tetracycline (3 μg mL^{-1}) was applied in the subsequent tests, with the reference of the peak blood-drug concentration (2–4 μg mL^{-1}, 2 h following administration) or the drug concentration in the gingival crevice fluid (0.61 μg mL^{-1}) in clinical practice against periodontitis.[32]

2.11. *In vitro* bactericidal ability of ZnO_2–Fe_3O_4@MV NPs

First, TSB at pH 5.0 was prepared with acetic acid–sodium acetate buffer solution. The bacterial suspension of *S. gordonii* was collected by centrifugation at 1500*g* for 5 min, washed twice with 1× PBS and resuspended in TSB (pH 5.0) to a concentration of 1×10^8 CFU mL^{-1}. One hundred microliters of *S. gordonii* suspension in TSB was mixed with 100 μL of 1× PBS, tetracycline, ZnO_2@Fe_3O_4 NPs and ZnO_2–Fe_3O_4@MV NPs (final dilutions of 0, 3, 100 and 100 μg mL^{-1}, respectively) and the obtained mixture was incubated for 2 h at 37 °C. After incubation, 0.1 mL aliquots were serially diluted in TSB, plated onto TSA agar and cultured for 24 h at 37 °C before enumeration of CFUs.

In addition, *S. gordonii* was mixed in TSB (pH 5.0) obtained by the above steps with different concentrations of ZnO_2–Fe_3O_4@MV NPs (0, 10, 20, 50, 100, 200, 500 and 1000 μg mL^{-1}), the obtained mixture was then incubated for 2 h at 37 °C. 0.1 mL aliquots were serially diluted in TSB, plated onto TSA agar and cultured for 24 h at 37 °C before enumeration of CFUs.

2.12. Preparation of Lipo@DiI and SG MVs@DiI

Lipo@DiI was prepared using a mixture of EPC (100 μL, 9.9 mg mL^{-1}) and DiI (1 μL) by referring to the standard liposome preparation with a film hydration/extrusion method.[33] The mixture was dried in a vacuum oven overnight at room temperature. Then, Lipo@DiI was suspended in filtered 1× PBS and extruded 20 times through a 400 nm polycarbonate membrane.

S. gordonii MVs were incubated with 5 μM DiI for 30 min. Excess DiI was removed *via* ultracentrifugation at 10 000*g* for 5 min at 4 °C.

2.13. Uptake assessment of *S. gordonii* MVs

The uptake of SG MVs@DiI or Lipo@DiI was evaluated in planktonic *S. gordonii* and *P. gingivalis* cultured to 1×10^8 CFU mL^{-1}. The bacteria (3 mL) were incubated with the same volume of SG MVs@DiI or Lipo@DiI (1 mL) for 2 h, followed by centrifugation for 5 min at 1500*g* to remove supernatants. The bacteria were labelled with Syto9 (5 μM) and incubated at 37 °C for 30 min. After incubation, they were washed with 1× PBS and dripped into a confocal dish. Fluorescent images were acquired using a Zeiss LSM 800 confocal microscope with a 63× magnification lens. A laser with an excitation wavelength of 565 nm was used to visualize the excitation/emission wavelengths including 549/565 nm for DiI and 488/503 nm for Syto9.

In addition, flow cytometry was used to analyze the internalization efficiency of SG MVs@DiI or Lipo@DiI in bacteria. The bacteria were collected by centrifugation at 1500*g* for 5 min after co-incubation with SG MVs@DiI or Lipo@DiI, and analyzed with a C6 Plus flow cytometer and FlowJo software.

2.14. Culture of symbiotic biofilms

Symbiotic biofilms were cultured on round glass cover slides with a diameter of 18 mm in 12-well plates for follow-up experiments. Briefly, the collected *S. gordonii* (10^8 CFU mL^{-1}) was marked for 40 min with HI (15 μg mL^{-1}) at 37 °C. After incubation, the unbound fluorescent dye was removed by centrifugation and resuscitated to 10^9 CFU mL^{-1} with TSB (adding 0.8 g mL^{-1} glucose and yeast extract). Next, 1 mL of bacterial suspension was added to each well of the 12-well plate and placed at 37 °C for 2 h. The biofilm culture plates were wrapped in aluminum foil to protect stained bacteria from light. The culture medium and unadhered bacteria were slowly removed, replaced with TSB, and then cultured for 20 h.

P. gingivalis (10^8 CFU mL^{-1}) was washed and labelled with the 5(6)-FAM fluorescent dye (5 μg mL^{-1}) for 40 min. After incubation, the unbound fluorescent dye was removed by centrifugation (850*g*, 3 min) and resuscitated to 10^9 CFU mL^{-1} with TSB. When *S. gordonii* biofilms were cultured for 16 h, the supernatant was removed and replaced with a stained *P. gingivalis* suspension. They were cultured at 37 °C in an anaerobic environment for 24 h to form symbiotic biofilms. Glass cover slips with biofilms were used for further experiments.

2.15. Reactive oxygen species (ROS) detection

ROS levels were determined using a 2′7′-dichlorodihydrofluorescein diacetate (DCFH-DA) probe. The *S. gordonii* bacterial suspensions were resuspended to 1×10^7 CFU mL^{-1} in a pH 5.0 medium. They were incubated with PBS, tetracycline, ZnO_2–Fe_3O_4 NPs and ZnO_2–Fe_3O_4@MV NPs (finally diluted to 0, 3, 100 and 100 μg mL^{-1}) for 2 h and then incubated with DCFH-DA (2 mL, 5 μM) in the dark at 37 °C for 15 min. The residual DCFH-DA probe was removed by centrifugation, washed three times with 1× PBS, and then dropped in a confocal dish for fluorescence imaging. Fluorescence images of DCFH-DA were recorded at excitation and emission wavelengths of 488 nm and 525 nm.

In addition, flow cytometry was used to analyze the level of bacterial intracellular ROS production. After different treatments as specified, *S. gordonii* samples were incubated with DCFH-DA (2 mL, 5 μM) in the dark at 37 °C for 15 min, followed by centrifugation (1500*g*, 3 min) for collection. Then the samples were loaded for experiments with the C6 Plus flow cytometer and analyzed with FlowJo software.

After the culture of symbiotic biofilms for 48 h, the supernatants were replaced with a pH 5.0 medium. They were

diluted with PBS, tetracycline, ZnO_2–Fe_3O_4 NPs and ZnO_2–Fe_3O_4@MV NPs (finally diluted to 0, 3, 100 and 100 μg mL^{-1}) for 2 h. Then, DCFH-DA (2 mL, 5 μM) was incubated in the dark at 37 °C for 15 min. Residual DCFH-DA probes were removed by centrifugation (1000*g*, 3 min) and washed three times with PBS. The round glass slides were then transferred to a confocal dish for fluorescence imaging.

2.16. Symbiotic biofilm eradication by ZnO_2–Fe_3O_4@MV NPs

In vitro biofilm eradication was tested on symbiotic biofilms on glass in a 12-well plate. The supernatants were removed and replaced with pH 5.0 TSB at different concentrations, in which the concentrations of tetracycline, ZnO_2–Fe_3O_4 NPs and ZnO_2–Fe_3O_4@MV NPs were set as 3, 100 and 100 μg mL^{-1}, respectively. After incubation for 2 h, the culture media were removed. A Zeiss LSM 800 confocal microscope was used to acquire fluorescence images for biofilm evaluation. Each group of experiments were repeated by using three samples (n = 3) in parallel. The blank control group was treated with 1× PBS.

The images obtained by confocal microscopy were analyzed with the ImageJ software. Briefly, the areas of interest were transferred to 8-bite type grayscale images. Then, the threshold was adjusted to select all positive signals to obtain the average optical density value (IntDen/area) in the images. The term of IntDen/area was defined by the integrated optical density values over pixels of the area above the threshold for each biofilm image at different fluorescence channels.

2.17. Symbiotic biofilm eradication on prosthesis mouse gingival tissue sections

Male BALB/C mice (7 weeks old) were provided by the Model Animal Research Center of Soochow University (Suzhou, China). All experiments (study number 22024344) were performed in accordance with the guidelines and with the approval of the Institutional Animal Care and User Committee at Soochow University. The gums of the newly executed mice were cut off, washed with 1× PBS, transferred to −80 °C and frozen for 2 h. Using a Leica frozen slicer, the gingival tissue was cut into thin slices with a thickness of 80 μm and then affixed to the bottom of the confocal dish. The prepared tissue slice samples were first treated with the Tissue AutoFluo Quencher for 10 min and cleaned with 1× PBS 3 times to eliminate the influence of tissue spontaneous fluorescence on subsequent fluorescence imaging. Gingival tissue prosthesis was used to culture symbiotic biofilms of *S. gordonii* and *P. gingivalis* in a similar procedure. The culture time of the *S. gordonii* biofilms was shortened to 12 h. Then, deposition of *P. gingivalis* was performed for the co-culture of symbiotic biofilms for another 12 h. The media were replaced by the addition of different concentrations of tetracycline, ZnO_2–Fe_3O_4 NPs and ZnO_2–Fe_3O_4@MV NPs (3, 100 and 100 μg mL^{-1}, respectively). The blank control group was treated in the medium, with 1× PBS replacing antibiotics or nanocomposites. Fluorescence images were acquired according to the methods described as above. The method of image processing using ImageJ software was the same as that shown above.

2.18. Statistical analysis

The experimental data are expressed as mean ± SD. The data were analysed using the one-way ANOVA method, with the standard setting (***$p < 0.001$, **$p < 0.01$, and *$p < 0.05$).

3. Results and discussion

3.1. Preparation and characterization of ZnO_2–Fe_3O_4@MV NPs

ZnO_2 nanoparticles were synthesized by mixing $Zn(OAc)_2$ and H_2O_2 at room temperature in the presence of PVP. Fe_3O_4 nanoparticles were prepared by a solvothermal method using $Fe(acac)_3$ as the precursor. After surface modification of Fe_3O_4 NPs with DHCA, electrostatic interactions were employed to assemble core–shell structured ZnO_2/Fe_3O_4 nanocomposites. As shown in Fig. S1,† dynamic light scattering data were acquired in aqueous suspensions of nanoparticles, suggesting uniform size distributions of ZnO_2 NPs (70 ± 10 nm), Fe_3O_4 NPs (5 ± 2 nm), and ZnO_2/Fe_3O_4 NPs (80 ± 10 nm). TEM micrographs revealed the morphological features of Fe_3O_4 anchored on the surface of ZnO_2 NPs (Fig. 1a). The coating layer of *S. gordonii* MVs on the surface of ZnO_2/Fe_3O_4 NPs was estimated to be a dozen of nanometers, based on the TEM micrograph (Fig. 1b) and the DLS measurements (Fig. S1a†). ZnO_2/Fe_3O_4@MV NPs exhibited a negative zeta potential of 19 mV approximately, which was favorable for their dispersity in aqueous solutions and against the re-adhesion of bacteria after the collapse of symbiotic biofilms by electrostatic repulsion.[34] HAADF-STEM and EDS mapping confirmed the existence and distribution of Fe, Zn, and N elements in ZnO_2–Fe_3O_4@MV nanocomposites (Fig. 1c and d). The X-ray diffraction (XRD) patterns of ZnO_2/Fe_3O_4 NPs and ZnO_2/Fe_3O_4@MV NPs were similar, indicating dominant contributions by ZnO_2 NPs in the composite nanomaterials (Fig. 1e). The XRD peaks derived from Fe_3O_4 were mostly masked, partly due to an overwhelming ratio between ZnO_2 and Fe_3O_4 in the nanocomposites. The typical peaks of Fe, Zn and O elements were present in the X-ray photoelectron spectrum (XPS) of the ZnO_2–Fe_3O_4@MV NPs (Fig. S2†). Among them, the peaks at 704.0 eV and 724.3 eV were attributed to Fe $2p_{3/2}$ and Fe $2p_{1/2}$, and the peaks at 1029.6 eV and 1053.3 eV were assigned to Zn $2p_{3/2}$ and Zn $2p_{1/2}$, respectively, while the asymmetric doublet at 529.6 eV and 531.9 eV was correlated to O 1s derived from Fe–O and Zn–O.[29,35–37] In the Fourier transform infrared (FT-IR) spectra of ZnO_2–Fe_3O_4 NPs and ZnO_2–Fe_3O_4@MV NPs, the vibration of carbonyl group (C═O) stretching was indicated by the peak at 1732 cm^{-1}, considering the contribution by the proteins and lipids due to MV coating (Fig. S3†). The transmittance decreases in the region of 1360–1030 cm^{-1} indicating the elevated vibrations of the C–N bond in ZnO_2–Fe_3O_4@MV NPs due to the presence of MVs (Fig. S3†). The contents of Fe_3O_4 NPs and ZnO_2 NPs in the ZnO_2–Fe_3O_4@MV

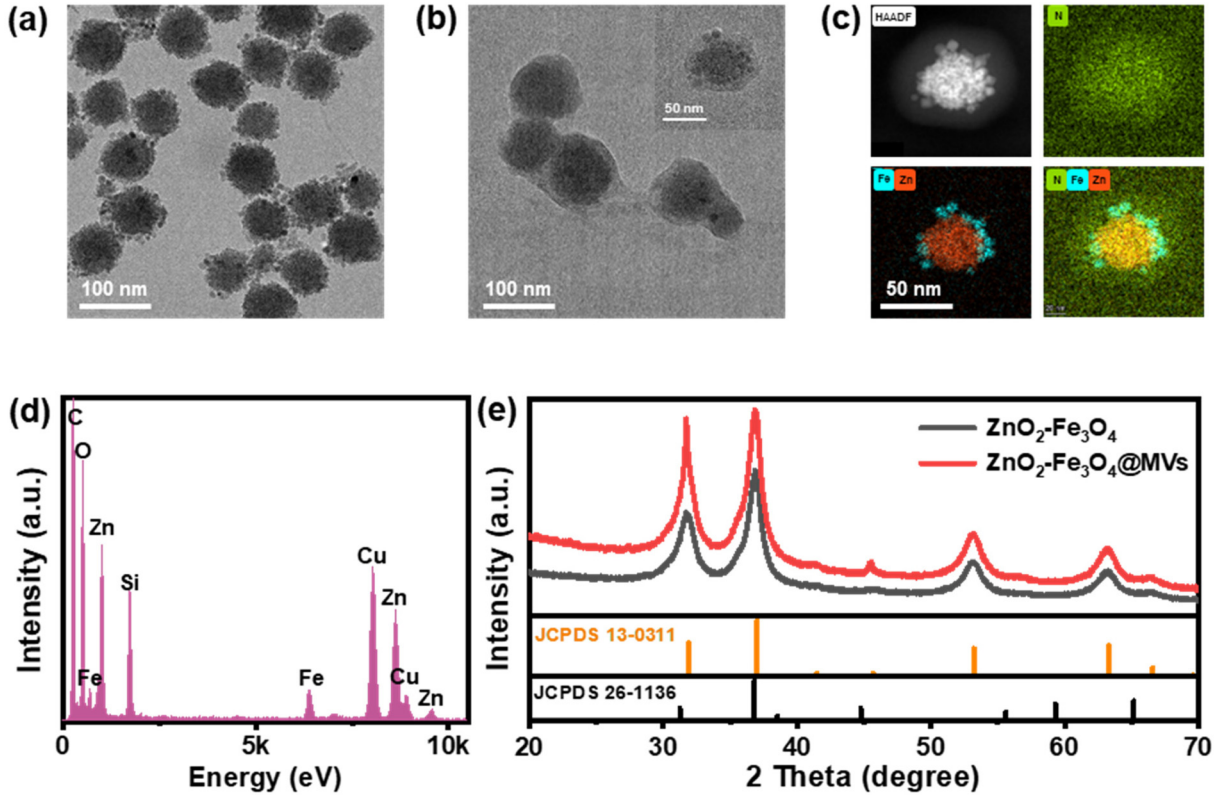

Fig. 1 Characterization of ZnO_2–Fe_3O_4 NPs and ZnO_2–Fe_3O_4@MV NPs. (a) TEM image of ZnO_2–Fe_3O_4 NPs, scale bar: 100 nm. (b) TEM image of ZnO_2–Fe_3O_4 NPs coated with *S. gordonii* membrane vesicles, scale bar: 100 nm. Inset: zoomed-in view of ZnO_2–Fe_3O_4@MV NPs, scale bar: 50 nm. (c) High-angle annular dark-field (HAADF) scanning TEM image of a single ZnO_2–Fe_3O_4@MV NPs, and energy-dispersive X-ray spectroscopy mapping of Fe, Zn, and N elements, scale bar: 50 nm. (d) Electronic differential system spectrum of ZnO_2–Fe_3O_4@MV NPs. (e) Powder X-ray diffraction spectra of ZnO_2–Fe_3O_4 NPs and ZnO_2–Fe_3O_4@MV NPs. The standard card of ZnO_2 (JCPDS: 13-0311) and Fe_3O_4 (JCPDS: 26-1136).

NPs were quantitatively analyzed by inductively coupled plasma-mass spectrometry (ICP–MS) and determined to be 26.7% and 73.3%, respectively. PAAM gel electrophoresis was employed to separate membrane proteins in the samples involving MV coating. As shown in Fig. S4,† the bands of bare SG MVs and ZnO_2–Fe_3O_4@MV NPs resembled each other in the protein profiles, while the band of ZnO_2–Fe_3O_4 NPs was mostly blank. The gel electrophoresis data also suggested that the extrusion step in the preparation of membrane coated nanocomposites can maintain most of the membrane proteins. Collectively, these results suggested the successful synthesis of ZnO_2–Fe_3O_4@MV nanocomposites.

3.2. Highly efficient generation of $^{\bullet}OH$ *via* the Fenton reaction

The releasing behaviours of Zn and Fe ions from ZnO_2–Fe_3O_4@MV NPs were measured with ICP-MS under neutral (pH 7.4) and acidic (pH 5.0) conditions. As shown in Fig. 2a and b, the acidic buffer solution (pH 5.0) was obviously more favourable for the rapid releasing of both Zn and Fe ions from the composite nanomaterials. After incubation of 24 h, 63% of Zn content and 60% of Fe content were released into the buffer solution at pH 5.0. In contrast, the release of Zn or Fe ions was much slower in the neutral buffer, tending to reach a plateau after 24 h. Approximately 25% of Zn content and 20% of Fe content were detected in the buffer solution at pH 7.4 outside the dialysis membrane. These results suggested the acid-responsive decomposition of ZnO_2–Fe_3O_4@MV NPs, while maintaining a good stability when suspended in the neutral buffer.

A commercial hydrogen peroxide detection kit was employed to detect the H_2O_2 production capacity of ZnO_2 NPs in gradient pH buffer solutions (pH 5.0, 5.5, 6.5, and 7.4) within 2 h incubation. After the calibration with the standard curve, the colorimetric data suggested that the maximal amount of H_2O_2 was at the level of 0.29 mg H_2O_2 per mg ZnO_2 NPs at pH 5.0 in 2 h (Fig. S5†).

Fe_3O_4 nanoparticles can convert H_2O_2 produced by ZnO_2 NPs into highly active $^{\bullet}OH$ *via* the Fenton reaction under acidic conditions. The efficiency of the Fenton reaction using our H_2O_2 self-supplied Fe_3O_4 co-assembled NPs was monitored with a typical probe of 3,3′,5,5′-tetramethylbenzidine (TMB). The UV-vis absorption spectra of TMB incubated with ZnO_2–Fe_3O_4@MV NPs featured the peak intensity changes at 370 and 652 nm. In the neutral buffer (pH 7.4), there was no detectable changes at these two wavelengths. Decreasing the pH values in the buffer solutions from 7.4 to 4.5 was consistently accompanied with elevated absorption peaks at 370 and

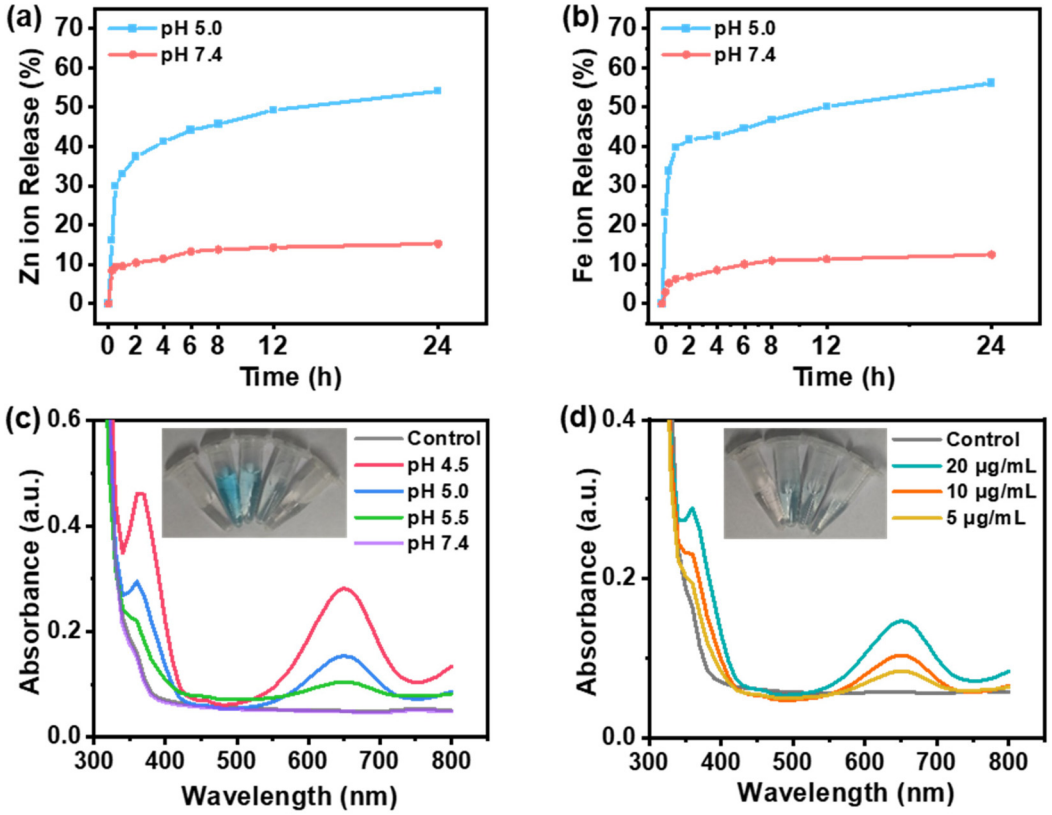

Fig. 2 Ion release and catalytic activity evaluation of ZnO_2–Fe_3O_4@MV NPs. The release profiles of (a) Zn and (b) Fe ions in suspended ZnO_2–Fe_3O_4@MV NPs. Concentration: 2 mg mL^{-1}; dialysis bags: MD77. (c) UV-vis spectra and pictures of TMB solutions (inset) after incubation with 20 μg mL^{-1} ZnO_2–Fe_3O_4@MV NPs in different pH buffers. (d) UV-vis spectra and pictures of TMB solutions (inset) after incubation with various concentrations of ZnO_2–Fe_3O_4@MV NPs at pH 5.0 buffer.

652 nm (Fig. 2b). Our experiments also verified that the absorption peak changes were dependent on the concentrations of ZnO_2–Fe_3O_4@MV NPs (Fig. 2c). Collectively, ZnO_2–Fe_3O_4@MV NPs can rapidly produce H_2O_2 under acidic conditions to fuel the Fenton reaction, simultaneously generating highly toxic $^{\bullet}OH$ with catalysis by Fe_3O_4 NPs or the released Fe ions.

3.3. Enhanced uptake of SGMV coated cargos by *S. gordonii*

S. gordonii was incubated with DiI-labelled MVs (SG MVs@DiI) or DiI-labelled liposomes (Lipo@DiI) for 2 h to investigate the interactions between bacteria and MVs. Then the fluorescent dye Syto9 was quickly applied to label both living and dead *S. gordonii*. As shown in Fig. 3a, the co-localized fluorescent signals between the Syto9 channel (green) and DiI channel (red) indicated the uptake patterns of MVs by *S. gordonii* (shown in yellow in the merged image panel). As a negative control, there were little colocalized fluorescent signals in the *S. gordonii* incubated with Lipo@DiI. In addition, there was almost no signal of free DiI dye molecules delivered in the aqueous solution internalized by *S. gordonii* (Fig. 3a). Semi-quantitative analysis was performed to compare the fluorescence images by calculating the percentagewise pixel ratios of the co-localized fluorescence to the Syto9 staining, or to the DiI staining, alternatively. The results suggested that the bacterial uptake efficiency of *S. gordonii* MVs was higher than that of liposomes by 5 folds, when normalized with Syto9 fluorescence (Fig. 3b). The utilization rate of *S. gordonii* MVs was higher than that of liposomes by 3 folds, when normalized with DiI fluorescence (Fig. 3c). In addition, the flow cytometry data validated that more than 80% of *S. gordonii* were positive with DiI labelling by the method of MV delivery, while only 32% was positive with DiI labelling by the method of liposomes (Fig. S6†). Therefore, *S. gordonii* MVs were much more efficient than conventional liposomes at delivering cargos to the target bacteria.

We also attempted to test the uptake of SG MVs by *P. gingivalis* (Fig. S7a†). The experimental results suggested that the uptake efficiency of SG MVs by *P. gingivalis* (Fig. S7a and b†) was lower than that by *S. gordonii* (Fig. 3a and b) under the identical conditions. Similarly in the control experiments, *P. gingivalis* tended to internalize less Lipo@DiI than SG MVs (Fig. S7b and c†). The difference in the uptake of membrane vesicles and liposomes by *P. gingivalis* was confirmed by the flow cytometry data (Fig. S8†). Membrane vesicles could be uptaken by bacteria *via* membrane fusion or endocytosis, where the similarity of the components and protein–receptor interactions play a pivotal role in the rate-con-

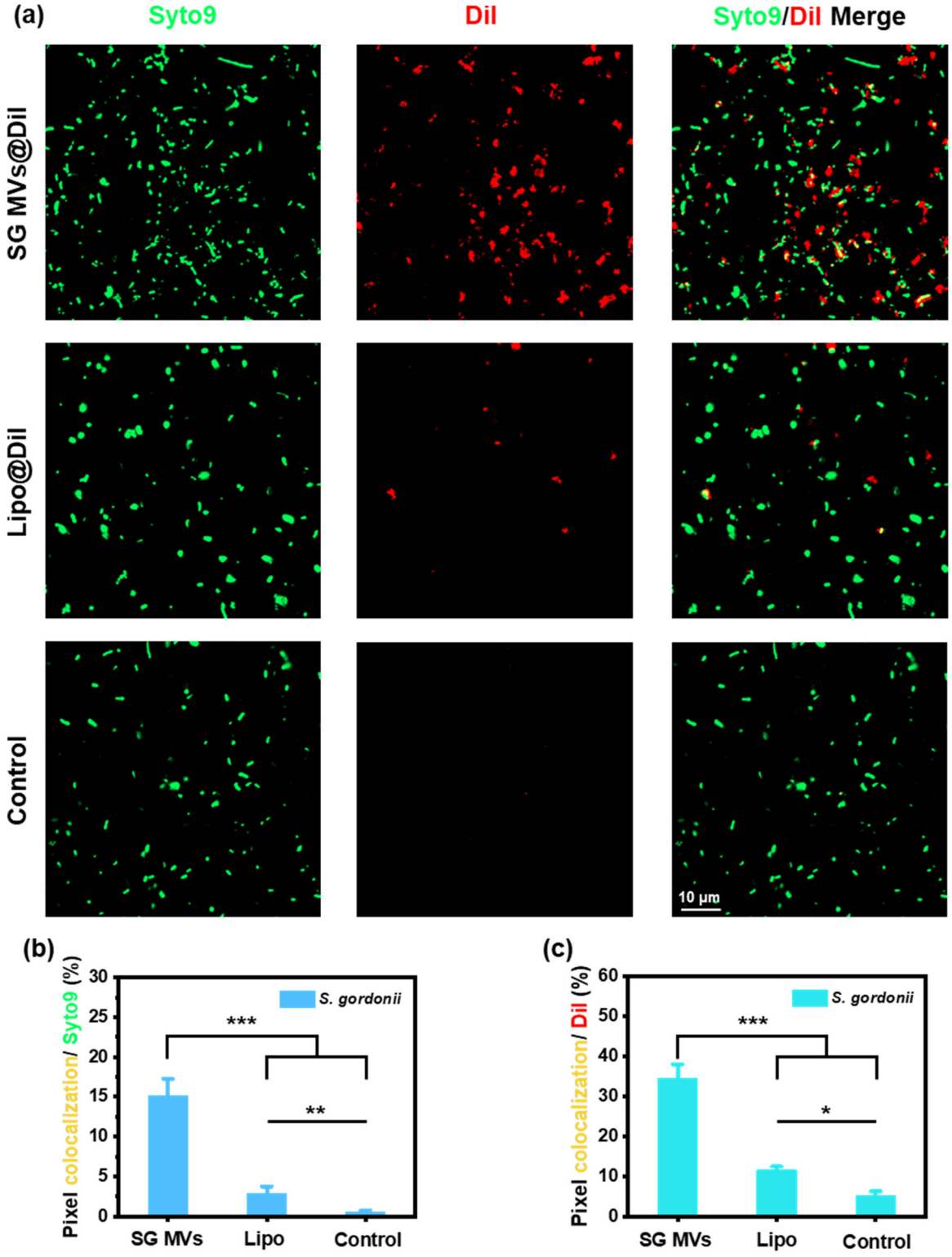

Fig. 3 Confocal fluorescence images of *S. gordonii* incubated with *S. gordonii* MVs and image analysis. (a) Confocal fluorescence images of *S. gordonii* incubated with SG MVs@DiI, Lipo@DiI, and PBS control for 2 h. Green fluorescence: *S. gordonii* stained with Syto9, E_m: 488 nm; red fluorescence: *S. gordonii* MVs and liposomes stained with DiI, E_m: 565 nm. Yellow: merge of green and red. Scale bar: 10 μm. (b) The area ratios of colocalized pixels of both green and red normalized by the pixels of green (Syto9). (c) The area ratios of colocalized pixels of both green and red normalized by the pixels of red (DiI). Error bar: standard deviation (n = 3). Statistical significance by one-way analysis of variance (*p < 0.05, **p < 0.01, ***p < 0.001).

trolling step. Our experiments quantified the distinct uptake preferences of bacteria when choosing natural membrane vesicles and synthetic liposomes. Interestingly, the difference of bacteria belonging to separate phyla in uptaking membrane vesicles was revealed by our method. The parental targeting and accessibility of membrane vesicles have natural advantages over conventional liposome or hydrogel drug delivery systems, allowing the contents to accumulate near the target bacteria. The special colonization relationship between *S. gordonii* and *P. gingivalis* provides a new possibility for the mass uptake of SGMV coated nanotherapeutics in basal bacteria, to induce the "Jenga-style" collapse of the biofilm system and clearance of less abundant pathogens.

3.4. Inhibition of planktonic bacteria by ZnO_2–Fe_3O_4@MV NPs

We tested the killing effect of sZnO_2–Fe_3O_4@MV NPs at different concentrations on planktonic *S. gordonii* at pH 5.0. When the concentration of ZnO_2–Fe_3O_4@MV NPs reached 100 μg mL^{-1}, more than 90% of planktonic bacteria were eliminated. A further increase in the concentration of ZnO_2–Fe_3O_4@MV NPs did not significantly change the killing effect on planktonic *S. gordonii* (Fig. S9a†). Then, we evaluated the anti-bacterial performance of ZnO_2–Fe_3O_4@MV NPs and ZnO_2–Fe_3O_4 NPs at 100 μg mL^{-1}, including tetracycline at a minimal inhibitory concentration (MIC) of 3 μg mL^{-1} as the antibiotic control (Fig. S9b†). ZnO_2–Fe_3O_4 NPs dramatically reduced the survival rate of planktonic *S. gordonii* even better than the antibiotics, which was mainly attributed to the efficient production of $^{\bullet}OH$ in the Fenton reaction by the nanoparticles. Among these different treatments in shown Fig. S9b,† ZnO_2–Fe_3O_4@MV NPs suppressed the colony numbers of *S. gordonii* more than 10 folds better than the PBS control or more than 2 folds better than bare ZnO_2–Fe_3O_4 NPs, which was contributed by the enhanced bacterial uptake of nanocomposites with the strategy of *S. gordonii* membrane coating.

The biocompatibility of ZnO_2–Fe_3O_4@MV NPs on normal human derived cells, including HUVECs and 293T cells, was evaluated by the standard CTG assays. As shown in Fig. S10a,† ZnO_2–Fe_3O_4@MV NPs did not influence much of cell viabilities in these two normal cell lines below the final concentration of 100 μg mL^{-1}. After incubation with ZnO_2–Fe_3O_4@MV NPs (100 μg mL^{-1}) for 24 h, the cell viability of HUVECs or 293T cells remained 85%, or 86% respectively. When the concentration of ZnO_2–Fe_3O_4@MV NPs was increased to 200 μg mL^{-1}, the cell viability reduced to 73% for HUVECs, while dropped to 62% for 293T cells. Briefly, ZnO_2–Fe_3O_4@MV NPs featured good biocompatibility in the tests of normal cells below the concentration of 100 μg mL^{-1}. In addition, we evaluated the biosafety of ZnO_2–Fe_3O_4@MV NPs with murine-derived cells, including L929 cells, 3T3 cells, and RAW 264.7 cells. As shown in Fig. S10b,† after incubation with ZnO_2–Fe_3O_4@MV NPs at the concentration of 100 μg mL^{-1} for 24 h, the cell viability of L929 cells, 3T3 cells and RAW 264.7 cells remained 88%, 86% and 90%, respectively. The results verified the good cellular biocompatibility of ZnO_2–Fe_3O_4@MV NPs.

3.5. Effect of ZnO_2–Fe_3O_4@MV NPs on biofilm dispersal *in vitro*

A symbiotic biofilm model of *S. gordonii* and *P. gingivalis* was constructed to evaluate the anti-biofilm effect of ZnO_2–Fe_3O_4@MV NPs with our "Jenga-style" strategy. The other control treatments included ZnO_2–Fe_3O_4 NPs without coating of *S. gordonii* MVs, tetracycline, and PBS as the blank control. As shown in Fig. 4a, there was a dense layer of biofilms (35 nm in thickness) growing on the glass substrate after culture for 48 h. The PBS treatment did not influence the symbiosis of *S. gordonii* (labelled with red) and *P. gingivalis* (labelled with green), as evidenced by the large area of colocalization (shown in orange) of these two bacterial staining. As a regular antibiotic against anaerobic bacteria, tetracycline reduced the growth of *S. gordonii*, relatively inferior to its effect on *P. gingivalis*, which might be attributed to the differences in anaerobic and drug sensitiveness between these two types of bacteria. However, the biofilms remained in a large portion on the substrate in detectable thickness (Fig. 4a). The effect on biofilm inhibition by ZnO_2–Fe_3O_4 NPs was better than that by tetracycline. It suggested that active $^{\bullet}OH$ generated by ZnO_2–Fe_3O_4 NPs *via* the Fenton reaction was effective at suppressing both *P. gingivalis* and *S. gordonii*. Most strikingly, ZnO_2–Fe_3O_4@MV NPs decomposed the symbiotic biofilms by the removal of *S. gordonii* and depletion of *P. gingivalis*. Given the fact that *S. gordonii* was cultured as the layer of foundation of symbiotic biofilms, comparison of the results in Fig. 4a validated that our "Jenga-style" strategy with ZnO_2–Fe_3O_4@MV NPs was outstandingly successful in the combats against the robust biofilms.

Integrated fluorescence intensities normalized by pixel areas were acquired by the *z*-axis scanning of all the image cubes, including indices at the HI channel for *S. gordonii* and the 5(6)-FAM channel for *P. gingivalis* in the symbiotic biofilms (Fig. 4b and c). Then the peak areas of the curves in Fig. 4b and c can be calculated for comparison of the total amounts of each bacterium remaining in the biofilms after these treatments (Fig. S11†). The treatment of ZnO_2–Fe_3O_4@MV NPs featured thorough removal of *P. gingivalis* and *S. gordonii* (minimal peak areas in Fig. S11†), thus leading to reduced biofilm thickness in comparison to the other control treatments.

In addition, the DCFH-DA probe was used to examine the bacterial killing effect of $^{\bullet}OH$ generated by ZnO_2–Fe_3O_4 NPs or ZnO_2–Fe_3O_4@MV NPs in planktonic *S. gordonii* (Fig. S12 and S13†) and the biofilms (Fig. S14†). Overall, the results of both tests were consistent with each other. Different from the PBS or tetracycline treatment, there were obvious fluorescence signals of the DCFH-DA probe in the reaction with $^{\bullet}OH$ from *S. gordonii* treated with ZnO_2–Fe_3O_4 NPs. The signals of DCFH-DA probe became even more intensive when bacteria were treated with ZnO_2–Fe_3O_4@MV NPs, indicating more efficient generation of $^{\bullet}OH$ *in situ* (Fig. S12–S14†).

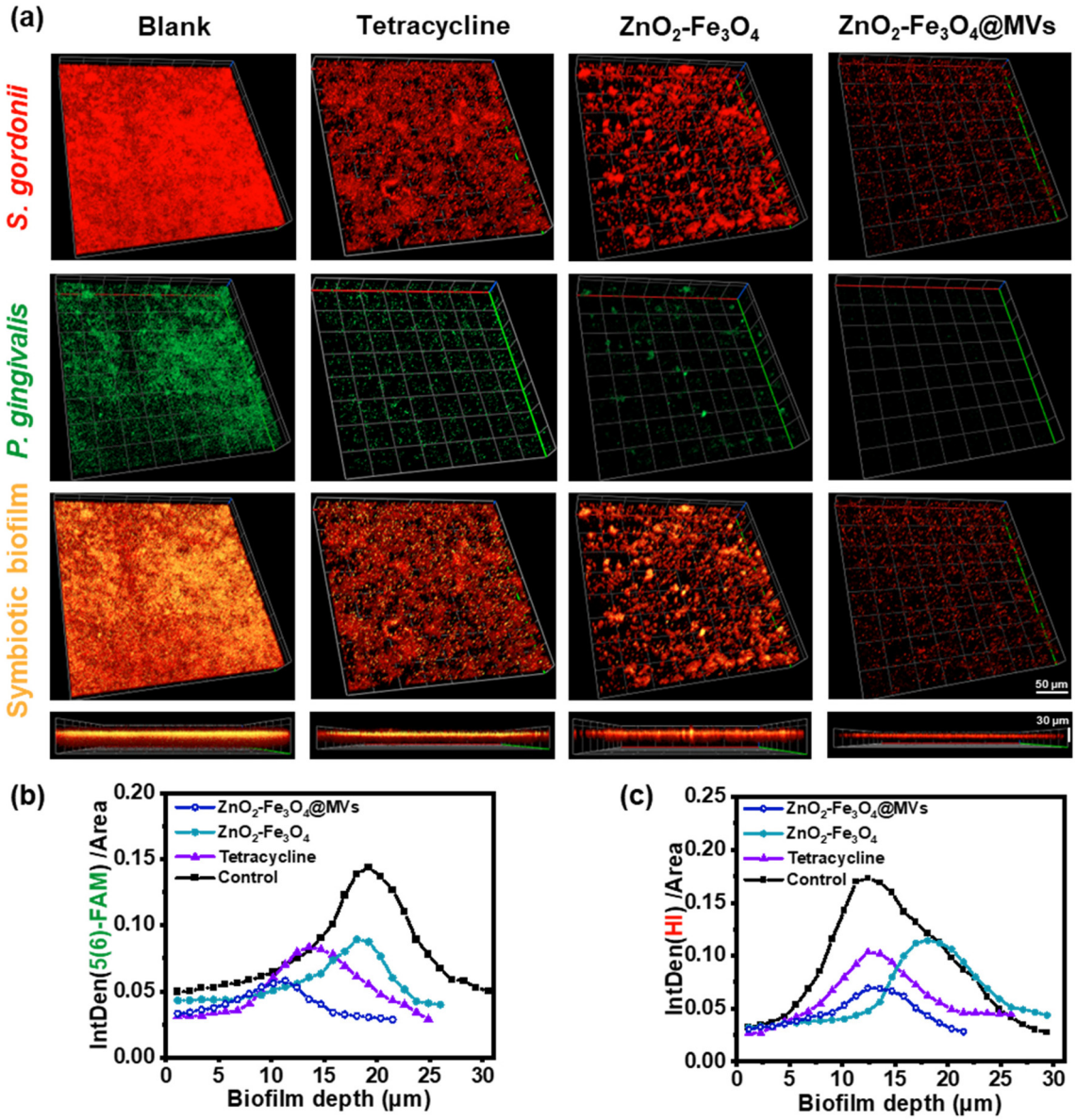

Fig. 4 Influence on *S. gordonii* and *P. gingivalis* symbiotic biofilms by different treatments of PBS, tetracycline, ZnO_2–Fe_3O_4 NPs, or ZnO_2–Fe_3O_4@MV NPs. (a) CLSM images of remaining biofilms after the specified treatments at the following fluorescent channels: *S. gordonii* pre-stained with HI (red, E_m: 600 nm); *P. gingivalis* stained with 5(6)-FAM (green, E_m: 521 nm). Orange: merge of green and red. Scale bar: 100 μm. Integrated fluorescence densities normalized by pixel areas of (b) 5(6)-FAM and (c) HI from the *z*-axis scanning of the biofilms.

3.6. "Jenga-style" collapse of symbiotic biofilms by ZnO_2–Fe_3O_4@MV NPs on mouse gingival tissue sections

An *ex vivo* model of the symbiotic biofilms of *P. gingivalis* and *S. gordonii* on mouse gingival tissue sections was developed for the purpose of evaluation. The panel of Fig. 5a includes the fluorescence images acquired at the 5(6)-FAM channel for *P. gingivalis* (in green), HI channel for *S. gordonii* (in red), merged for both bacteria (in orange), and the bright-field images (in black-and-white) as the morphological reference of mouse gingival tissues. There was a thick and dense layer of symbiotic biofilms left on the tissue sections with the treatment of PBS only. The treatment of tetracycline suppressed bacterial growth by the inhibition of peptide chain elongation and protein synthesis. Consistent with our previous observation (Fig. 4a), a difference in bacterial survival between *P. gingivalis* and *S. gordonii* suggested that the effects of tetracycline were dependent on bacterial types (Fig. 5a). The damage on symbiotic biofilms prepared with mouse gingival tissues became enlarged by the treatment of ZnO_2–Fe_3O_4 NPs, due to the generation of highly toxic $^{\bullet}OH$. The anti-biofilm effect of ZnO_2–Fe_3O_4@MV NPs was outstanding by damaging *S. gordonii* most and removing *P. gingivalis*. The fluorescence staining intensities of both

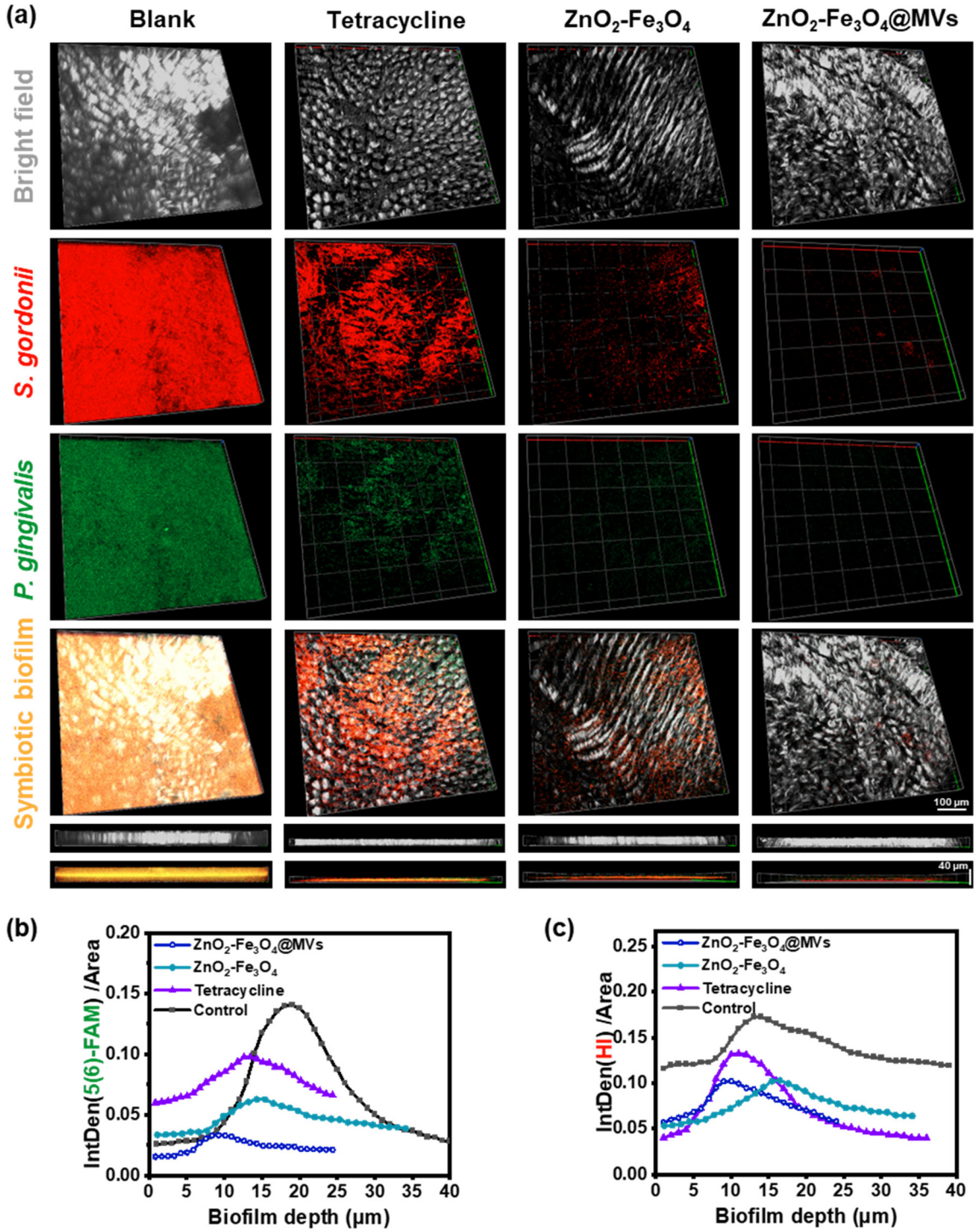

Fig. 5 Influence on *S. gordonii* and *P. gingivalis* symbiotic biofilms by different treatments of PBS, tetracycline, ZnO_2–Fe_3O_4 NPs, or ZnO_2–Fe_3O_4@MV NPs on the mouse gingival tissue sections (*ex vivo*). (a) Bright-field and CLSM images of remaining biofilms after the specified treatments at the following fluorescent channels: *S. gordonii* pre-stained with HI (red, E_m: 600 nm); *P. gingivalis* stained with 5(6)-FAM (green, E_m: 521 nm). Orange: merge of green and red. Scale bar: 100 μm. Integrated fluorescence densities normalized by the pixel areas of (b) 5(6)-FAM and (c) HI from the *z*-axis scanning of the biofilms.

bacteria were analysed by *z*-axis scanning (Fig. 5b and c and Fig. S15†), which verified the anti-biofilm differences by these treatments described as above.

Different from conventional therapies against periodontitis in clinics (*e.g.*, antibiotics; optionally assisted by physical treatments), our method was not relied on any antibiotics, thus

avoiding typical consequences of antibiotic resistance.[38] Instead, our nanomaterials featured self-supplied H_2O_2 and efficient generation of $^{\bullet}OH$ *via* the Fenton reaction by nano-catalysts. They can be delivered onto periodontal-disease-associated biofilms, with enhanced uptake/cleanse of *S. gordonii* due to our special MV coating (Fig. 3 and 4). According to the statistical data of periodontitis in clinics, *S. gordonii* is counted as a dominant species in oral bacteria (3.21% of total clones), while *P. gingivalis* occupies 0.29% of total clones (more than 10 folds fewer than *S. gordonii*).[39] Some other types of bacteria may also rely on the colonization site created by *S. gordonii* during the biofilm formation in the oral cavity, such as *Fusobacterium nucleatum*, *Actinomyces oris* and *Veillonella atypica*, which can increase the biofilm robustness in a whole and improve the survival conditions of opportunistic pathogens.[40–42] Our strategy focuses on damaging *S. gordonii* with a high priority, which allows for the effective destruction of the pathogenic biofilms in a "Jenga-style", including *P. gingivalis* or opportunistic pathogens. Given the fact that *S. gordonii* served as the foundation bacteria of periodontitis biofilms, any severe damage on *S. gordonii* eventually amplified to a crushing blow of the symbiotic biofilms in a "Jenga" style. Our experiments demonstrated that ZnO_2–Fe_3O_4@MV NPs can induce severe disruption of *S. gordonii*, thus leading to the clearance of colonized *P. gingivalis* colonization and the collapse of periodontitis symbiotic biofilms (Fig. 5). To the our best knowledge, this work represents the first report of "Jenga-style" treating pathogenic symbiotic biofilms with a high efficacy.

The pilot *ex vivo* models of symbiotic biofilms on tissue sections established in this work was useful for translational research. The traditional methods of periodontitis based on rodent models suffered from several shortcomings: longer period of modelling (over 6 weeks), interference by rodent individual drinking/eating habits, large numbers of animal sacrifices, and difficulty in microscopic real-time monitoring. In contrast, we developed a new method to prepare symbiotic biofilms on rodent gingival tissue sections. It allowed us to perform any tests on the symbiotic bacteria combinations in a highly selective and controllable manner. The preparation time to co-culture symbiotic biofilms can be reduced to one day. The inherently better optical transparency of sectioned tissues made it much easier to acquire microscopic images in real-time. The sectioned gingival tissues not only provided nutrient supplies partly for colonization of bacteria, but also served as quasi three-dimensional substrates for symbiotic biofilms. Therefore, they could mimic the microenvironment of periodontitis pathogens better than bare glass substrates in the development of symbiotic biofilms for translation medical research. However, only a limited number of bacterial species (*S. gordonii* and *P. gingivalis*) were included in this *ex vivo* model, and their potential interactions with immune cells in the oral cavity were not taken into consideration yet. Due to these limitations, the *ex vivo* model shall be utilized as an additional evaluation tool to test any specific combinations of bacterial biofilms, instead of using it as a replacement for the *in vivo* tests.

4. Conclusions

We have developed a "Jenga-style" method to treat periodontitis symbiotic biofilms by using ZnO_2/Fe_3O_4@MV NPs. Different from conventional therapies using systemic antibiotics or broad-spectrum nano therapeutics, our method features selectively targeted delivery/damage of the foundational bacteria (*S. gordonii*) with ZnO_2/Fe_3O_4@MV NPs, followed by collapse of the symbiotic biofilms for thorough clearance. Our data from flow cytometry and fluorescence microscopy suggest that SGMV coatings allow enhanced uptake of cargos by *S. gordonii* preferably more than *P. gingivalis*. The *in vitro* and *ex vivo* experiments have validated the high efficacy of this "Jenga-style" anti-biofilm strategy. It promises a new method to control different bacterial types/abundances in symbiotic biofilms for translational medicine.

Author contributions

Cao Q., Shi R. and Liu J. conceived and designed the experiments. Cao Q. and Shi R. synthesized materials. Cao Q., Xiao X., Tao C., Guo R. and Li X. performed cell culture, bacterial culture and flow cytometry experiments. Cao Q., Shi R. and Lv R. evaluated the *in vitro* and *ex vivo* biofilm efficacy. Cao Q., Shi R. and Liu J. wrote the manuscript. Cao Q., Shi R., Sui B., Liu X. and Liu J. analyzed the data and revised the paper. All the authors contributed to the paper.

Conflicts of interest

The authors declare that they have no known competing financial interests.

Acknowledgements

This project was funded by the National Key Research and Development Program of China (2017YFE0131700), the National Natural Science Foundation of China (21874096), the 111 project, the Joint International Research Laboratory of Carbon-Based Materials and Devices, the Collaborative Innovation Center of Suzhou Nano Science, and the Suzhou Key Laboratory of Nanotechnology and Biomedicine.

References

1 J. L. Pathak, Y. Yan, Q. Zhang, L. Wang and L. Ge, *Respir. Med.*, 2021, **185**, 106475.
2 N. B. Parahitiyawa, L. J. Jin, W. K. Leung, W. C. Yam and L. P. Samaranayake, *Clin. Microbiol. Rev.*, 2009, **22**, 46–64.
3 B. Rosan and R. J. Lamont, *Microbes Infect.*, 2000, **2**, 1599–1607.
4 D. A. Siddiqui, A. B. Fidai, S. G. Natarajan and D. C. Rodrigues, *Dent. Mater.*, 2022, **38**, 84–396.

5 B. L. Pihlstrom, B. S. Michalowicz and N. W. Johnson, *Lancet*, 2005, **366**, 1809–1820.
6 G. Hajishengallis, S. Liang, M. A. Payne, A. Hashim, R. Jotwani, M. A. Eskan, M. L. McIntosh, A. Alsam, K. L. Kirkwood, J. D. Lambris, R. P. Darveau and M. A. Curtis, *Cell Host Microbe*, 2011, **10**, 497–506.
7 R. P. Darveau, *Nat. Rev. Microbiol.*, 2010, **8**, 481–490.
8 S. Yachida, S. Mizutani, H. Shiroma, S. Shiba, T. Nakajima, T. Sakamoto, H. Watanabe, K. Masuda, Y. Nishimoto, M. Kubo, F. Hosoda, H. Rokutan, *et al.*, *Nat. Med.*, 2019, **25**, 968–976.
9 S. S. Dominy, C. Lynch, F. Ermini, M. Benedyk, A. Marczyk, A. Konradi, M. Nguyen, U. Haditsch, D. Raha, C. Griffin, L. J. Holsinger, S. Arastu-Kapur, S. Kaba, A. Lee, *et al.*, *Sci. Adv.*, 2019, **5**, eaau3333.
10 P. N. Madianos, Y. A. Bobetsis and S. Offenbacher, *J. Periodontol.*, 2013, **84**, S170–S180.
11 A. Chopra, S. G. Bhat and K. Sivaraman, *J. Oral Microbiol.*, 2020, **12**, 1801090.
12 H. Rath, D. Feng, I. Neuweiler, N. S. Stumpp, U. Nackenhorst and M. Stiesch, *FEMS Microbiol. Ecol.*, 2017, **93**, fix010.
13 C. J. Rocco, L. O. Bakaletz and S. D. Goodman, *J. Bacteriol.*, 2018, **200**, e00790–17.
14 Y. Park, M. R. Simionato, K. Sekiya, Y. Murakami, D. James, W. Chen, M. Hackett, F. Yoshimura, D. R. Demuth and R. J. Lamont, *Infect. Immun.*, 2005, **73**, 3983–3989.
15 P. Slezak, M. Smiga, J. W. Smalley, K. Sieminska and T. Olczak, *Int. J. Mol. Sci.*, 2020, **21**, 4150.
16 S. K. Hansen, P. B. Rainey, J. A. Haagensen and S. Molin, *Nature*, 2007, **445**, 533–536.
17 R. Cosgarea, S. Eick, S. Jepsen, N. B. Arweiler, R. Juncar, R. Tristiu, G. E. Salvi, C. Heumann and A. Sculean, *Sci. Rep.*, 2020, **10**, 16322.
18 Y. Wang, Y. Yang, Y. Shi, H. Song and C. Yu, *Adv. Mater.*, 2020, **32**, 1904106.
19 G. Jiang, S. Liu, T. Yu, R. Wu, Y. Ren, H. C. van der Mei, J. Liu and H. J. Busscher, *Acta Biomater.*, 2021, **123**, 230–243.
20 F. Gao, X. Li, T. Zhang, A. Ghosal, G. Zhang, H. M. Fan and L. Zhao, *J. Controlled Release*, 2020, **324**, 598–609.
21 F. S. Atkinson, J. H. Khan, J. C. Brand-Miller and J. Eberhard, *Nutrients*, 2021, **13**, 2711.
22 L. Hong, S. H. Luo, C. H. Yu, Y. Xie, M. Y. Xia, G. Y. Chen and Q. Peng, *Pharm. Nanotechnol.*, 2019, **7**, 129–146.
23 X. Pang, D. Li, J. Zhu, J. Cheng and G. Liu, *Nano-Micro Lett.*, 2020, **12**, 144.
24 V. Marchiano, M. Matos, E. Serrano-Pertierra, G. Gutierrez and M. C. Blanco-Lopez, *Int. J. Pharm.*, 2020, **585**, 119478.
25 W. Huang, L. Meng, Y. Chen, Z. Dong and Q. Peng, *Acta Biomater.*, 2020, **140**, 102–115.
26 R. Shi, Z. Dong, C. Ma, R. Wu, R. Lv, S. Liu, Y. Ren, Z. Liu, H. C. van der Mei, H. J. Busscher and J. Liu, *Small*, 2022, **18**, e2204350.
27 X. Liu, Y. Sun, S. Xu, X. Gao, F. Kong, K. Xu and B. Tang, *Theranostics*, 2019, **9**, 5828–5838.
28 W. Huang, Q. Zhang, W. Li, M. Yuan, J. Zhou, L. Hua, Y. Chen, C. Ye and Y. Ma, *J. Controlled Release*, 2020, **317**, 1–22.
29 L. S. Lin, J. F. Wang, J. Song, Y. Liu, G. Zhu, Y. Dai, Z. Shen, R. Tian, J. Song, Z. Wang, W. Tang, G. Yu, Z. Zhou, Z. Yang, T. Huang, G. Niu, H. H. Yang, Z. Y. Chen and X. Chen, *Theranostics*, 2019, **9**, 7200–7209.
30 L. Cheng, K. Yang, Y. Li, J. Chen, C. Wang, M. Shao, S. T. Lee and Z. Liu, *Angew. Chem., Int. Ed.*, 2011, **50**, 7385–7390.
31 I. Wiegand, K. Hilpert and R. E. Hancock, *Nat. Protoc.*, 2008, **3**, 163–175.
32 D. Sakellari, J. M. Goodson, S. S. Socransky, A. Kolokotronis and A. Konstantinidis, *J. Clin. Periodontol.*, 2000, **27**, 53–60.
33 G. Fuhrmann, A. Serio, M. Mazo, R. Nair and M. M. Stevens, *J. Controlled Release*, 2015, **205**, 35–44.
34 X. T. Chu, F. P. Yang and H. Y. Tang, *Chin. J. Chem.*, 2022, **40**, 2988–3000.
35 T. Yamashita and P. Hayes, *Appl. Surf. Sci.*, 2008, **254**, 2441–2449.
36 H. Song, L. Zhu, Y. Li, Z. Lou, M. Xiao and Z. Ye, *J. Mater. Chem. A*, 2015, **3**, 8353–8360.
37 Y. Zhang, W. Liu, Y. Huang, Y. Wang, X. Chen and Z. Chen, *Chem. Eng. J.*, 2022, **446**, 137214.
38 T. H. Grossman, *Cold Spring Harbor Perspect. Med.*, 2016, **6**, a025387.
39 P. S. Kumar, E. J. Leys, J. M. Bryk, F. J. Martinez, M. L. Moeschberger and A. L. Griffen, *J. Clin. Microbiol.*, 2006, **44**, 3665–3673.
40 J. L. M. Welch, B. J. Rossetti, C. W. Rieken, F. E. Dewhirst and G. G. Borisya, *Proc. Natl. Acad. Sci. U. S. A.*, 2016, **25**, E791–E800.
41 T. J. Liu, R. Q. Yang, J. N. Zhou, X. J. Lu, Z. J. Yuan, X. Wei and L. H. Guo, *Front. Cell. Infect. Microbiol.*, 2022, **11**, 783323.
42 M. Lof, M. M. Janus and B. P. Krom, *J. Fungi*, 2017, **3**, 40.